Supporting Information

Room-Temperature Low-Threshold Lasing From Monolithically Integrated Nanostructured Porous Silicon Hybrid Microcavities

Valentina Robbiano,[†] Giuseppe M. Paternò,[‡] Antonino A. La Mattina,[†] Silvia G. Motti,[‡] Guglielmo Lanzani,[‖‡] Francesco Scotognella,[‖‡] and Giuseppe Barillaro[†]*

[†] Dipartimento di Ingegneria dell'Informazione, Università di Pisa, Via G. Caruso 16, 56122, Pisa, Italy

[‡] Center for Nano Science and Technology@PoliMi, Istituto Italiano di Tecnologia, Via Giovanni Pascoli, 70/3, 20133 Milano, Italy

[‖] Dipartimento di Fisica, Politecnico di Milano, Piazza Leonardo da Vinci 32, 20133 Milano, Italy

SECTION 1 – MORPHOLOGICAL CHARACTERIZATION OF PSi LAYERS AND MICROCAVITIES

The preparation of high quality PSi photonic structures, namely distributed Bragg reflectors (DBRs) and microcavities, requires a fine tuning of both porosity and thickness of PSi layers. In fact, porosity can be easily varied by changing the etching current density applied and, specifically, higher porosity can be obtained with higher current densities; once the etching current density is given, the thickness can be varied by changing the etching time. Both porosity and thickness values were evaluated from experimental reflectance spectra of PSi layers prepared at different etching current densities and etching times using a computational model that take into account both number and position of Fabry-Perot fringes occurring in the reflectance spectrum over the measured spectral range[1]. Once the porosity of as-prepared PSi layers is estimated, the corresponding refractive index is calculated *via* the well-known effective medium approximation (EMA) using the Bruggemann's equation:

$$(1 - V_{Si})\frac{n_{air}^2 - n_{ps}^2}{n_{air}^2 + 2n_{ps}^2} + V_{Si}\frac{n_{Si}^2 - n_{ps}^2}{n_{Si}^2 + 2n_{ps}^2} = 0 \qquad (1)$$

where V_{Si} is the silicon volume fraction, (1-V_{Si}) is the volume of silicon removed during the etching (*i.e.* the porosity), n_{air} is the refractive index of air, n_{Si} is the refractive index of the silicon, and n_{ps} is the effective refractive index of the as-prepared PSi layer.

In Figure SI_1(a) we report the reflectance spectra of PSi layer with different porosities and thicknesses prepared by applying 8 different current densities for different etching times. The values of porosity and thickness obtained for each PSi layer are given in the table in Figure SI_1(b).

Once the relationship holding between porosity and thickness values and etching current density and time is known, PSiMCs operating in different spectral region can be prepared by simply changing the temporal period (with constant duty cycle) of the etching current density square-wave (Figure SI_1(c)), for a given pair of high and low porosity values. In particular, we found a linear correlation between PSiMC stop-bands center-wavelength and etching current density waveform temporal period, as shown in Figure SI_1(d).

(a)

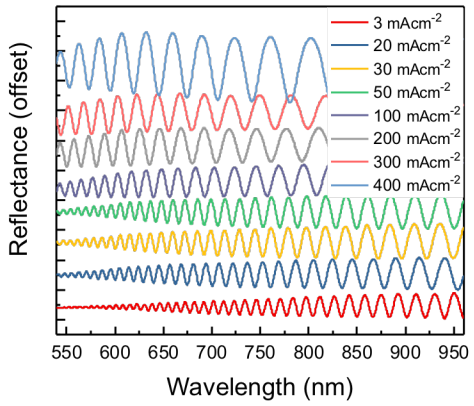

(b)

Current Density (mA/cm²)	Porosity (%)	Thickness (µm)	Etching time (s)
3	56	10.1	5000
20	59	8.1	750
30	60	7.9	500
50	60	7.9	300
100	66	6.5	150
200	72	5.9	75
300	75	5.6	50
400	77	5.5	37.5

(c)

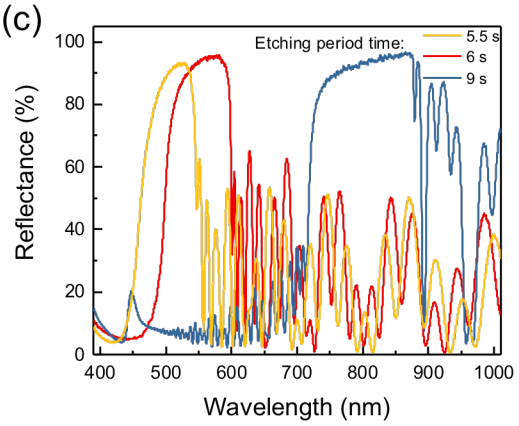

(d)

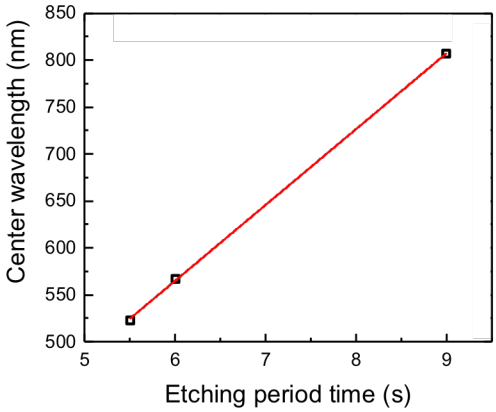

Figure SI_1 (a) Reflectance spectra (normalized, with a constant offset among them) of PSi layers prepared with different etching currents and etching times. (b) PSi morphological characteristics, namely porosity and thickness, calculated from the spectra shown in (a). (c) Reflectance spectra of PSiMCs prepared with etching current density square-wave with different period times. (d) Linear correlation between temporal period of the etching current density square-wave and center wavelength of the reflectance stop-band of the resulting PSiMCs.

In Figure SI_2(a) we report a high magnification SEM cross-section image of one of the DBR of the PSiMC discussed in Figure 1 of the main text, from which we extrapolated thickness of both high and low porosity PSi layers and of the bi-layer using ImageJ. A statistical analysis of the SEM image in Figure S1_2a resulted in a thickness of 76.9 ± 3.1 nm and 111.5 ± 8.1 nm for the low and high porosity layer, respectively, as reported in Figure SI_2(b). As a consequence, an interplanar

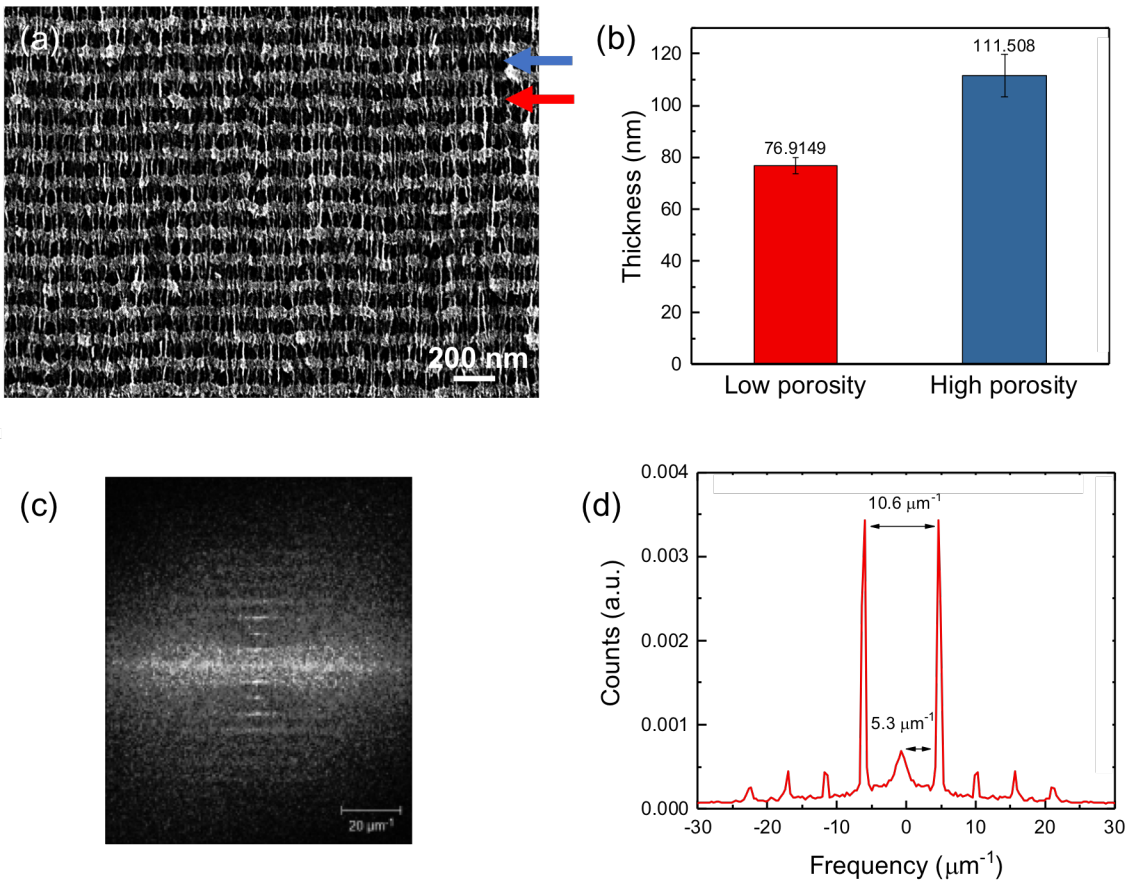

Figure SI_2 (a) High-magnification SEM cross-section image of one of the DBR of the PSi MC in Figure 1 of the main text. The red arrow points out a low porosity layer (brighter layers) and the blue arrow points out a high porous layer (darker layers). (b) Statistical estimation of the thickness of low (red) and high (blue) porosity layers are 76.91 and 111.51 nm, respectively. (c) 2D-FFT of (a). (d) Frequency profile extracted from the 2D-FFT in (c), highlighting a peak spacing of 5.3 μm^{-1} corresponding to a bi-layer spacing of 188 nm.

spacing (*i.e*. the thickness of the bi-layer) of ~188 nm was obtained. Such a value was further confirmed by 2-dimensional Fast Fourier Transform (2D-FFT) analysis of the SEM image in

Figure SI_2(a), which is reported in Figure SI_2(c). The FFT peaks spacing resulted 5.3 μm^{-1} (corresponding to 188 nm, Figure SI_2(d)), which is in perfect agreement to the outcome of the statistical image analysis.

SECTION 2 – SPECTROSCOPIC INVESTIGATION OF PSiMCs

In Figure SI_3(a) we report a photo of a PSiMC as-prepared (left) and after oxidation (right). The color changes from the green to the violet after oxidation, which is in agreement with the blue-shift of the stop-band of the microcavity upon oxidation.

Figure SI_3(c-d) shows bright field (c) and fluorescence (d) cross-section images of an on chip asymmetric PSiMC infiltrated with PFO, by comparison of which effective and uniform infiltration of PFO within the cavity can be appreciated. This is further confirmed by the

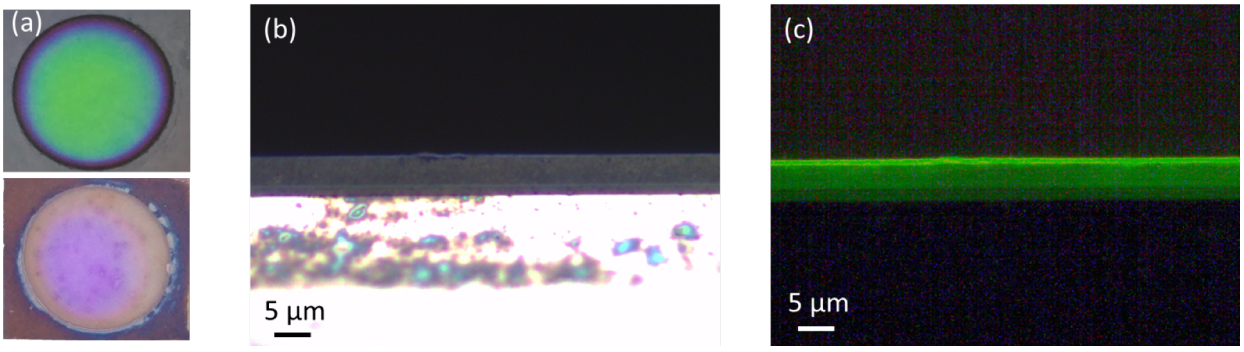

Figure SI_3 (a) Optical images of a PSiMC as-prepared (top) and after thermal oxidation (bottom). (b-c) Bright-field (b) and fluorescence (c) cross-section images of a PFO-infiltrated PSiMC on a silicon chip.

reflectance measurements of PSiMC before and after PFO infiltration reported in Figure 2 of the main text. The cross-section was obtained from PFO-infiltrated oxidised PSiMC still attached to the silicon substrate (*i.e.* before transfer-printing of the cavity on a PDMS slab), due to difficulties to cut PSiMCs once transfer-printed on PDMS slabs.

The presence of crystalline silicon (which shows high absorption in the visible region) underneath the cavity allows the fluorescence arising from the polymer infiltrated into the cavity itself to be better highlighted, with respect to the case of a PSi resonant cavity transfer-printed on a PDMS slab. Note that, polymer infiltration into a PSiMC still anchored to the silicon substrate represents a worst case in terms of polymer infiltration with respect to the case of PSiMC transfer-printed on a PDMS slab. In the latter, indeed, air trapped into the pores of the PSiMC can more easily exit from the bottom of the cavity as the polymer solution infiltrate the material.

Figure SI_4 shows theoretical reflectance and transmittance spectra calculated using the Transfer Matrix Method (TMM) for the PSiMC in Figure 1 of the main text at each preparation step, with the aim of corroborating experimental results of experimental spectroscopic characterization (Figure 2a of the main text). All theoretical calculations were all carried out reproducing exactly both structure and configuration of experimental measurements. The computational model gives rise to theoretical spectra that well agrees with experimental spectra. In particular, the theoretical reflectance spectrum of the as-prepared PSiMC (Figure SI4-1) was calculated using porosity values of 59% and 77% for the high and low refractive porosity layer, respectively, which are in perfect agreement with experimental values. The theoretical reflectance spectrum of the oxidised PSiMC (Figure SI4-2) was obtained using lower porosity values of 54% and 75%, which are in agreement with volume expansion, with respect to as-prepared PSi, of the porous structure after thermal oxidation due to conversion of silicon to silicon dioxide. A 0.3% of residual silicon in the

oxidised PSiMC resulted from theoretical calculation. For the calculation of theoretical reflectance and transmittance spectra of the PSiMC transfer-printed on the PDMS slab both before (Figure SI4-3) and after (Figure SI4-4) PFO-infiltration we used same porosity values as for the oxidised PSiMC. A 4% of PFO filing the air voids of the PSiMC resulted from theoretical calculations.

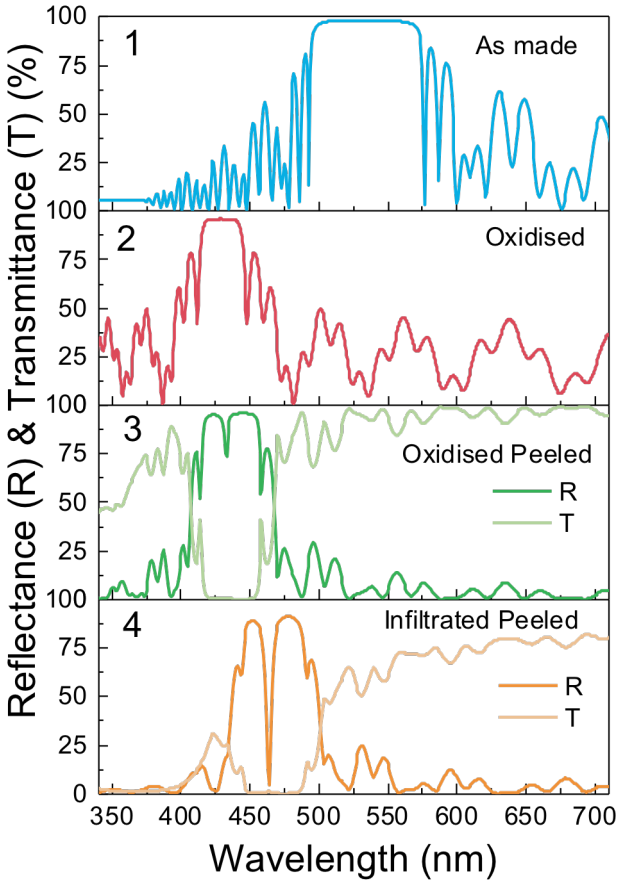

Figure SI_4 Calculated reflectance (R) and transmittance (T) spectra at each preparation step for the PSiMC of Figure 1a in the main text: 1 - reflectance spectra of the as-prepared PSiMC; 2 - reflectance spectra of the oxidized PSiMC; 3 - reflectance (dark green line) and transmittance (light green line) spectra of the PSiMC transfer-printed onto the PDMS slab; 4 - reflectance (dark orange line) and transmittance (light orange line) spectra of the PSiMC after PFO-infiltration.

SECTION 3 – SPECTROSCOPIC INVESTIGATION OF PFO AND PSi REFERENCE STRUCTURE

Figure SI_5(a) shows both absorption and PL spectra of PFO in solution, PFO thin-film on PDMS slab, and PFO infiltrated into the PSi reference structure.

Figure SI_5(b) shows the reflectance spectra of the PSi reference structure, from which it is apparent that it behaves as an interferometer.

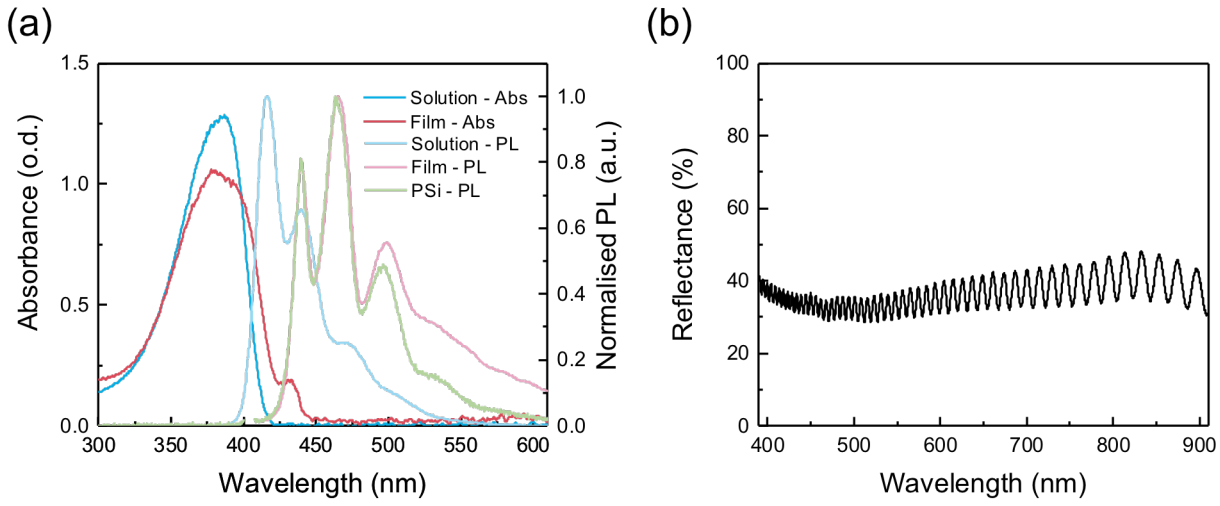

Figure SI_5 (a) Absorption and PL spectra of PFO solution (blue and light blue line) and PFO thin-film on PDMS slab (red and light red line), and PL spectrum of PFO infiltrated inside the reference PSi structure. (b) Reflectance spectrum of the reference PSi structure.

SECTION 4 – FERMI'S GOLDEN RULE AND RADIATIVE DECAY RATE

In the PSiMC the photonic density of state (p-DOS) is higher at the cavity mode wavelength, which results in an enhancement of the emission of the emitters located inside it, as predicted by the Fermi's golden rule:

$$R_{i\to f}(\omega) = \frac{2\pi}{\hbar}|\langle f|H'|i\rangle|^2\rho(\omega) \qquad (2)$$

where R is the transition probability from an initial state i to a finale state f that is related to the photon mean lifetime τ ($R = 1/\tau$), ρ is the density of final states, and $|\langle f|H'|i\rangle|^2$ is the matrix element of the perturbation H' between final and initial states.

In Figure SI_6 we note a very clear increase of the PL lifetime of the PFO emission in correspondence of the stop-band for the PSiMC with respect to the PSi reference.

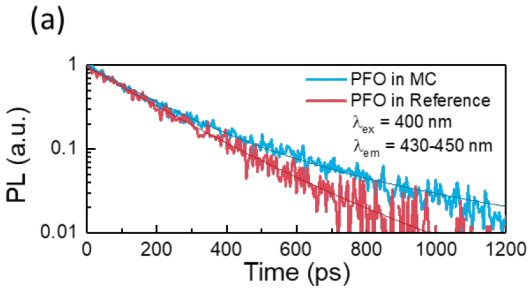

Sample	τ_1 (ps) (I_1)	τ_2 (ps) (I_2)	R^2
MC	**173** ± 7 (87.1)	**653** ± 14 (12.9)	0.991
Reference	**169** ± 9 (84.5)	**353** ± 21 (15.5)	0.988

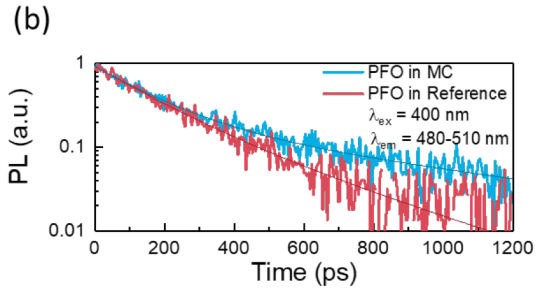

Sample	τ_1 (ps) (I_1)	τ_2 (ps) (I_2)	R^2
MC	**158** ± 10 (72.0)	**766** ± 25 (28.0)	0.977
Reference	**154** ± 8 (65.9)	**338** ± 29 (34.1)	0.976

Figure SI_6 Radiative decay of the PL in PFO-infiltrated PSiMC (blue line) and PSi reference structure (red line) recorded at wavelength within the microcavity photonic stop-band, namely λ_{em} between 430 and 450 nm (a) and between 480 and 510 nm (b). The time constants and the relative intensities are reported in the table in inset.

SECTION 5 – LASING EXPERIMENT SET-UP

Lasing experiments were carried out with an amplified Ti:sapphire laser at 400 nm with 2 mJ output energy and 2 kHz repetition rate. The laser power was set using a tunable optical density. The PSiMC was placed with the 30-bilayers stack facing the focused laser pump and the 10-bi-layers stack facing the collection lens, as schematically shown in Figure SI_7. The PSiMC was hold on a rotation stage that allowed a further control over the collection angle. Indeed, for the tuned PSiMC with resonant wavelength at 466 nm overlapping the PFO ASE emission we set the

collection collimating lens perpendicular to the sample surface, whereas for the red-shifted PSiMC with resonant wavelength at 591 nm the collection lens was oriented at 50° from the normal of the microcavity surface.

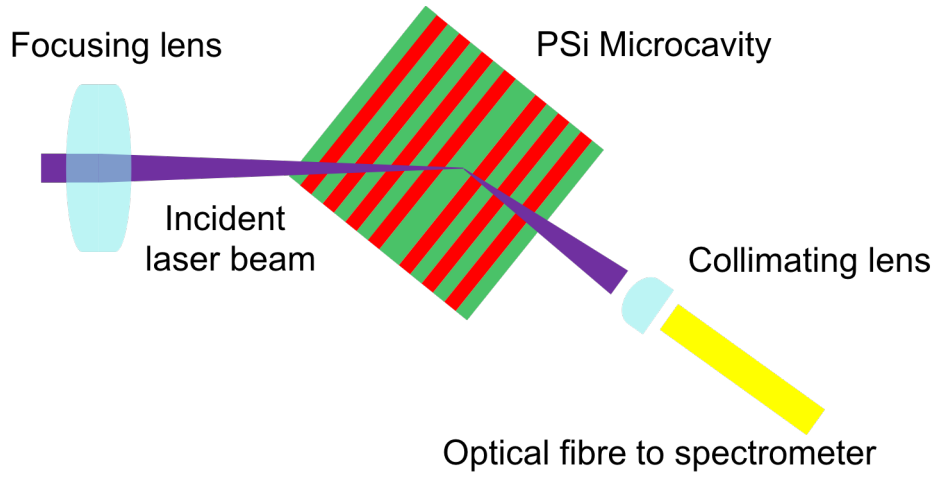

Figure SI_7 Scheme of the experimental setup used for lasing characterization of PSiMCs.

SECTION 6 – THEORETICAL ESTIMATION OF LASING THRESHOLD AND COHERENCE LENGTH

The lasing threshold can be evaluated as the ratio between the PL intensity of the stimulated emission, which occurs at the lasing wavelength, and the spontaneous emission, namely mode ratio in Figure SI_8. Below the threshold the mode ratio is close to unity. When the input power increases above the threshold, stimulated emission is dominating at the lasing wavelength and the mode ratio increases to about 10. The FWHM of the lasing mode, namely mode width in Figure SI_8, starts narrowing when the mode ratio is equal to two (indicated with a dashed line in Figure SI_8).

In order to validate the experimental lasing threshold, we calculated the theoretical threshold of our PSiMC hybrid laser.[2] The threshold condition is satisfied when the gain equals the losses in the microcavity, that is $\sigma Nl = \gamma$ where σ is the stimulated emission cross-section (7.6×10^{-16} cm^2 for PFO)[3], N is the upper level population, l is the length of the defect mode (~140 nm in our structure), and γ are the logarithmic losses. The latter parameter is determined as the ratio between the photon transit time inside the cavity (t_r) and photon lifetime in the cavity (τ_c)[4]: $\gamma = t_r/\tau_c$, with $t_r = nl/c$ (with n is the refractive index of the cavity defect (1.23) and c is the speed of light in vacuum) and $\tau_c = Q/2\pi\nu$ (with is the Q quality factor of the cavity and ν = 645 THz at 466 nm is the resonance frequency).

In our PSiMC we estimated that $t_r = 5.6\times10^{-16}$ s and $\tau_c = 1.9\times10^{-14}$ s, which lead to $\gamma = 2.9\times10^{-2}$. Being $\sigma = 7.6\times10^{-16}$ cm^2, then $Nl = 3.6\times10^{13}$ cm^{-2}.

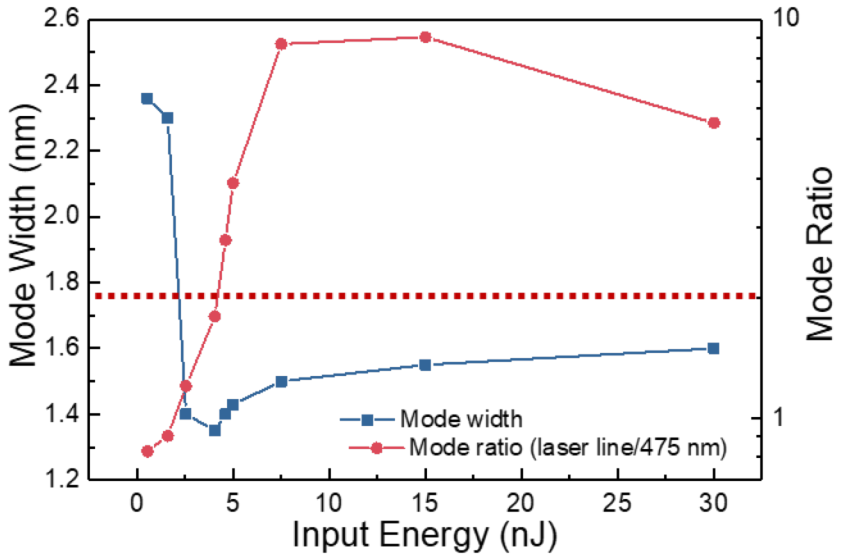

Figure SI_8 Mode width (FWHM) (red circles) and mode ratio (blue squares) of the lasing mode, the latter being calculated as power output ratio between lasing mode (λ=466 nm) and non-lasing mode (λ=4750 nm).

The corresponding pump fluence at the threshold is $F = Nlh\nu_p \sim 17$ J/cm^2, with h Plank's constant and ν_p pump frequency, which is in good agreement with the experimental data.

A rough estimation of the coherence length[5] of the lasing emission, ξ_{coh}, is obtained as $\xi_{coh} = \lambda_r^2/FWHM = 466^2/1.3 = \sim 0.17$ mm, where λ_r and FWHM are wavelength and width, respectively, of the laser line.

SECTION 7 – OPERATING STABILITY OF HYBRID PFO/PSiMC LASER

Figure SI_9 shows PL intensities (and PL spectra in inset) of PFO-infiltrated PSiMCs irradiated with an energy pump of 50 nJ, which is 10 times higher than the lasing threshold of 5 nJ, as a function of time (repetition rate 2kHz). After 6 min of operation (*i.e.* 7.2×10^5 pulses) the output PL intensity is decreased of ~40% of its initial values.

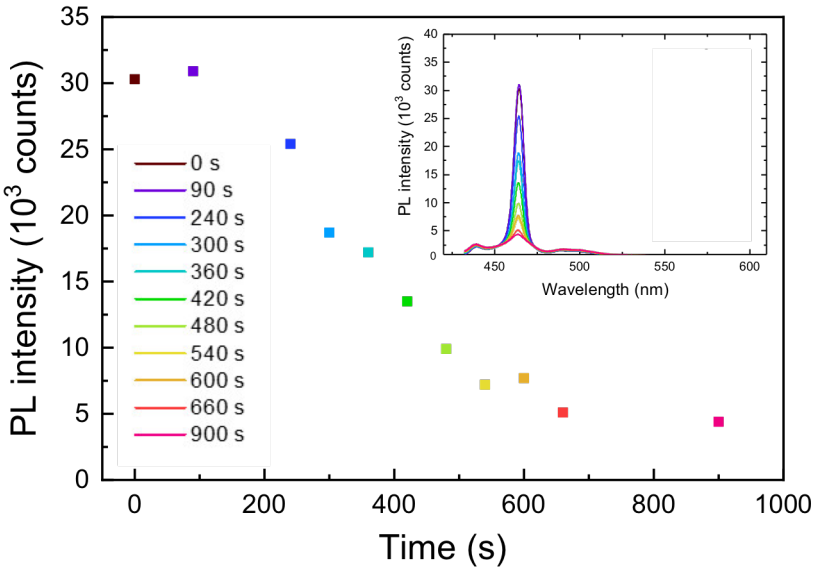

Figure SI_9 PL intensity of the PFO-infiltrated PSiMC at different operating time. Inset: PL spectra as a function of operating time.

SECTION 8 – SPECTROSCOPIC CHARACTERIZATION OF THE PFO-INFILTRATED PSi REFERENCE STRUCTURE

Figure SI_10 shows normalised PL spectra of the PFO-infiltrated PSi reference structure as a function of the pump power in the range 50 – 1600 nJ per pulse. The emission spectra were collected with same setup and cofiguration used for the lasing experiments with the PSiMC. It is apparent that by increasing the pump power there is no narrowing of the PL and the different spectra perfectly overlap.

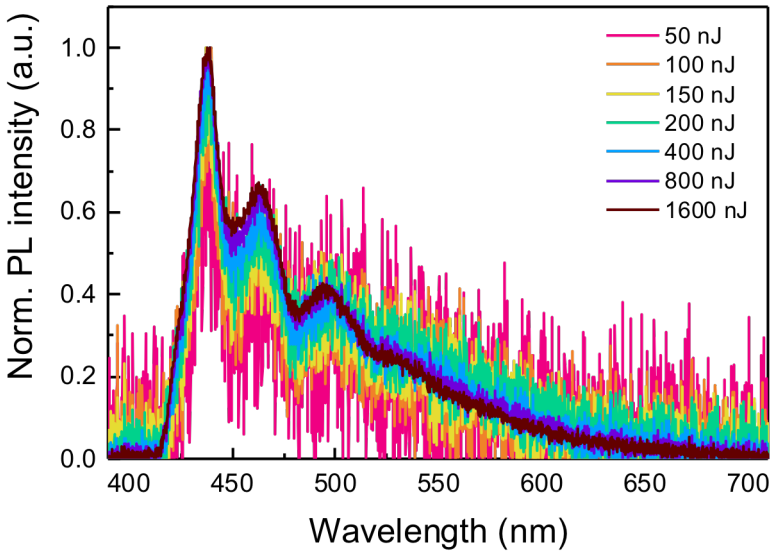

Figure SI_10 Normalised PL spectra of the PFO-infiltrated PSi reference structure at different input pump energies per pulse.

SECTION 9 – SPECTROSCOPIC CHARACTERIZATION OF THE RED-SHIFTED PSiMC

Figure SI_11(a) shows the reflectance spectrum collected at normal incidence (corresponding to a sample rotation of 0° in transmittance) of a PSiMC transfer-printed on a PDMS slab with a

resonance wavelength at 591 nm that is red-shifted with respect to PFO ASE. The PSiMC was prepared with same architecture and same etching parameters of the tuned microcavity (with resonance at 466 nm), though with an increased etching time period of 6.5 s.

Figure SI_11(b) shows angle-resolved transmittance spectra of the red-shifted PSiMC for 6 different collection angles. The optimal overlap between PFO emission and microcavity stop-band is reached at angles greater than 40°. The emission spectra of the PFO-infiltrated PSiMC collected at an angle of 50° for different input energy values are shown in Figure SI_11(c). Figure SI_11(d)

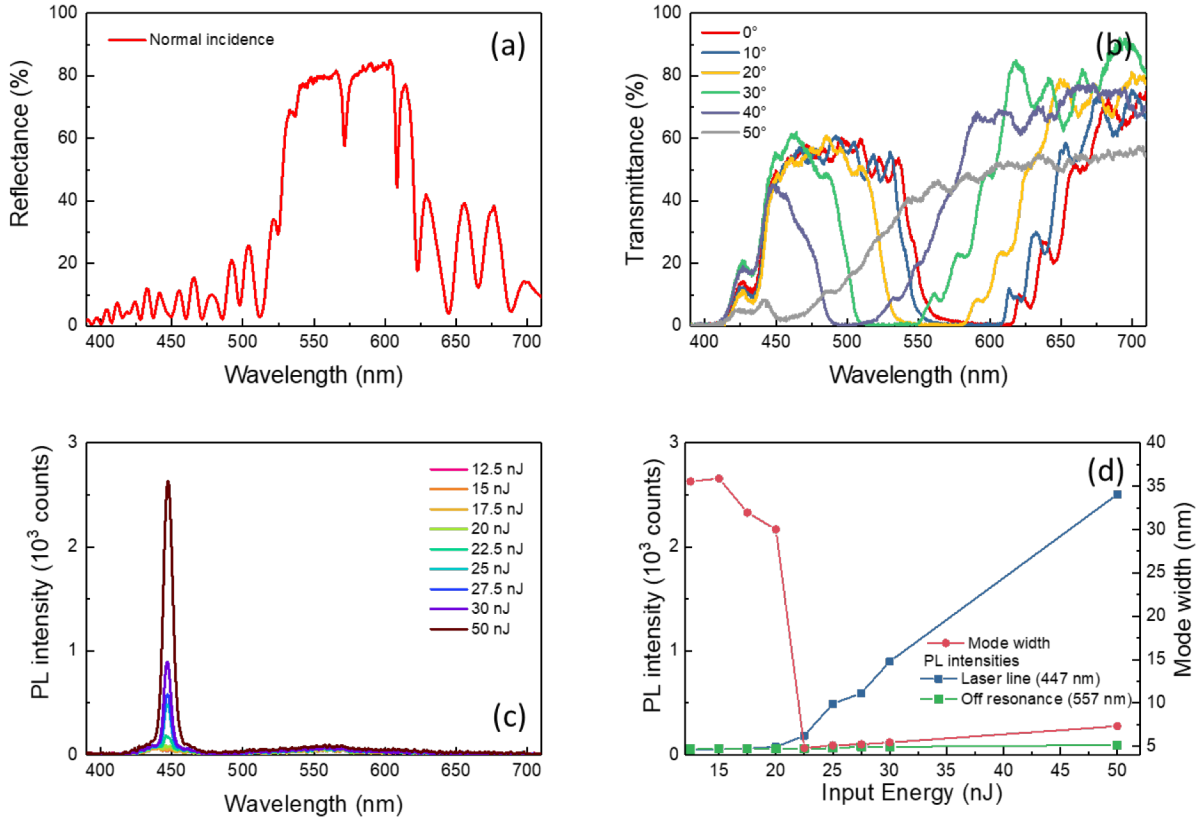

Figure SI_11 (a) Reflectance spectrum of a PFO-infiltrated PSiMC with resonance wavelength at 591 nm, probed at normal incidence. (b) Angle-resolved transmittance spectra of the PFO-infiltrated PSiMC in (a). (c) PL intensity spectra of the PFO-infiltrated PSiMC in (a) collected at 50° for different input energy per pulse values. (d) PF intensity (blue squares) and mode width (red circles) of the PFO-infiltrated PSiMC in (a) at the laser wavelength (447 nm), and PL intensity at a wavelength outside the cavity mode (557 nm) (green squares) for different input energy values.

reports PL intensity (blue squares) and mode width (red squares) of the red-shifted PSiMC at the lasing wavelength of 447 nm as a function of the different input energy values. Figure SI_11(d) also shows the PL intensity at 557 nm that is outside the cavity mode (green squares) versus input energy values. The PL intensity at the laser wavelength shows the characteristic input power threshold below which a linear increase is observed and above which a super-linear increase occurs. Conversely, the PL intensity at 557 nm always increase linearly with the input power and no threshold is observed. The lasing threshold obtained in this configuration (22.5 nJ) is higher than that of the tuned PSiMC, which can be explained with the reduced quality of the microcavity when collected at high incident angles.

REFERENCES

(1) Ruminski, A.M.; Barillaro G.; Chaffin C. and Sailor M.J. Internally Referenced Remote Sensors for HF and Cl_2 Using Reactive Porous Silicon Photonic Crystals. *Adv. Funct. Mater.* **2011**, 21, 1511-1525.

(2) Svelto, O.; Hanna, D. C. *Principles of Lasers*. Springer: New York, **1998**.

(3) Xia, R.; Heliotis, G.; Hou, Y.; Bradley, D. D. C. Fluorene-Based Conjugated Polymer Optical Gain Media. *Org. Electr.* **2013**, 4, 165-177.

(4) Zavelani-Rossi, M.; Perissinotto, S.; Lanzani, G.; Salerno, M.; Gigli, G; Laser Dynamics in Organic Distributed Feedback Lasers. Appl. Phys. Lett. **2006**, 89, 181105.

(5) Coles, H.; Morris, S. Liquid-Crystal Lasers. *Nat. Photon.* **2010**, 4, 676.